Contributions to Mineralogy and Petrology (2021) 176:66
https://doi.org/10.1007/s00410-021-01820-6

ORIGINAL PAPER

Experimental calibration of the reduced partition function ratios of tetrahedrally coordinated silicon from the Debye–Waller factors

Dongzhou Zhang[1] · Ming Chen[2] · Przemyslaw K. Dera[3] · Peter J. Eng[4]

Received: 12 October 2020 / Accepted: 17 July 2021

Abstract
We present a new *force constants* approach that combines experimental and theoretical data to constrain the reduced partition function ratio (β-factor) of tetrahedrally coordinated silicon (^{IV}Si) in the crust and upper mantle minerals. Our approach extends the experiment-based general moment approach, which relies on nuclear resonant scattering and is only applicable to Mössbauer-active elements, to Mössbauer-inactive elements such as Si. We determine the resilience of ^{IV}Si from the Debye–Waller factor, which is derived from the temperature dependence of single crystal X-ray diffraction data, and calculate the stiffness of ^{IV}Si from the density-functional theory results. The relationship between the resilience the stiffness is calibrated, and we have used an experimentally measurable parameter, the effective coordination number of the SiO_4 tetrahedron, to correct the stiffness. The correction is most pronounced for pyroxenes (~ 2%). The corrected stiffness is used to calculate the equilibrium isotope fractionation β-factor of each mineral, and the α-factors is calculated by taking the ratio of β-factors of different minerals. We calculate the $\ln\alpha_{Si30/28}$ between minerals that contains SiO_4 tetrahedra, and our results are consistent with DFT calculations and mass spectrometry results. Our results suggest that the Si isotopic equilibrium temperature between cristobalite and pyroxene in lunar basalt was underestimated by ~250 °C, and the pyroxene sample in IL-14 marble is in equilibrium with β-quartz.

Keywords Silicon · Isotope fractionation · Crystallography · X-ray diffraction

Introduction

Compared to primitive chondrites, the earth has unique fingerprints on its silicon isotope compositions (Georg et al. 2007; Shahar et al. 2009; Zambardi et al. 2013; Dauphas et al. 2015; Bourdon et al. 2018). Geochemistry studies have suggested that terrestrial samples are slightly enriched in the heavier isotope ^{30}Si relative to the chondrites, the raw materials that are most likely to have formed the earth (Georg et al. 2007; Shahar et al. 2009; Zambardi et al. 2013; Dauphas et al. 2015). The enrichment of ^{30}Si in the terrestrial samples provides constraints to many geochemical questions, including whether the earth's accretion material is chondritic (Fitoussi et al. 2009; Fitoussi and Bourdon 2012; Zambardi et al. 2013; Dauphas et al. 2015), whether there is an isotopically-light and hidden reservoir in the deep earth (Javoy et al. 2010; Huang et al. 2014; Georg et al. 2007; Shahar et al. 2009; Bourdon et al. 2018), and how much material was evaporated during the accretion of the earth and/or the moon-forming impact (Zambardi et al. 2013; Hin et al. 2017; Norris and Wood 2017).

The reduced partition function ratio (also known as the β-factor) is the key parameter to study the silicon isotope fractionation (Urey 1947; Bigeleisen and Mayer 1947; Polyakov and Mineev 2000; Polyakov 2009; Dauphas et al. 2012). The β-factor is defined as the equilibrium isotope fractionation factor between a compound and an ideal monoatomic gaseous reference (Urey 1947; Bigeleisen and Mayer 1947). Though the β-factor is not obtainable from

Communicated by Gordon Moore.

✉ Dongzhou Zhang
dzhang@hawaii.edu

[1] Hawaii Institute of Geophysics and Planetology, University of Hawaii at Manoa, Honolulu, HI 96822, USA

[2] Department of Chemistry, University of California and Materials Sciences Division, Lawrence Berkeley National Laboratory, Berkeley, CA 94720, USA

[3] Hawaii Institute of Geophysics and Planetology, University of Hawaii at Manoa, Honolulu, HI 96822, USA

[4] GSECARS, University of Chicago, Argonne, IL 60439, USA

Published online: 11 August 2021

mass spectroscopy, it is directly related to the equilibrium fractionation factor between two phases (the α-factor), which is experimentally measurable through mass spectrometry. The α-factor between two phases is calculated by taking the ratio of their respective β-factors (Méheut et al. 2007, 2009; Huang et al. 2014; Wu et al. 2015). Once the β-factor of each phase is accurately determined, one may calculate the isotope fractionation between different mineral phases at different P–T conditions (Méheut et al. 2007, 2009; Huang et al. 2014; Wu et al. 2015).

Several studies have been carried out to constrain the β-factors of silicon in minerals, and the majority of recent studies takes advantages of theoretical density-functional theory (DFT) calculations (e.g., Méheut et al. 2007, 2009; Schauble 2011; Méheut and Schauble 2014; Huang et al. 2014; Wu et al. 2015; Qin et al. 2016). DFT calculations of β-factors use the ground-state harmonic vibrational frequencies and the changes in phonon frequencies by isotopic substitution to calculate β-factor from the Bigeleisen–Mayer equation, and the calculated isotope fractionation matches mass spectrometry results reasonably well (Méheut et al. 2007, 2009; Schauble 2011; Méheut and Schauble 2014; Huang et al. 2014; Wu et al. 2015; Qin et al. 2016). On the other hand, DFT calculation has its own limitations. In DFT calculation, β-factors depend on the exchange-correlation energy functional (Méheut and Schauble 2014; Wu et al. 2015). A reliable calculation on the fractionation α-factor between minerals requires calculating the β-factors of both minerals with the same exchange-correlation energy (Méheut and Schauble 2014), which can be difficult for minerals with complex compositions and structures. Meanwhile, the calculations of the vibrational frequency are based on harmonic approximation at 0 K (Méheut et al. 2007, 2009; Méheut and Schauble 2014; Huang et al. 2014; Wu et al. 2015; Qin et al. 2016), and their accuracy under planetary conditions requires experimental validations. For example, one recent DFT calculation has not satisfactorily capture the temperature dependence of the Si isotope fractionation between silica and pyroxene (Méheut et al. 2009).

Compared to DFT calculations, experimental approach to determine the β-factors has its own advantages. Experimental approach does not require the quantum ground state approximation and the selection of exchange-correlation energy functionals, and can be carried out at the conditions of planetary interiors. Several studies used published vibrational spectra (e.g., Raman, infrared and rotational–vibrational spectroscopy) and force-field modeling to calculate the β-factor of O, Fe, Cl and Cr in different compounds, so as to constrain the equilibrium isotope fractionation (Kieffer 1982; Gillet et al. 1996; Polyakov 1998; Schauble et al. 2001, 2003, 2004). Recent experimental determination of the β-factor focuses on select Mössbauer-active elements like Fe, Sn, Eu and Kr (Polyakov and Mineev 2000; Polyakov 2009; Dauphas et al. 2012, 2018). One can either use the second order Doppler shift (Polyakov and Mineev 2000) or the Lamb–Mössbauer factor (Zhang et al. 2021) of the Mössbauer spectra, or use the partial phonon density of states (pDOS) derived from the nuclear resonant inelastic X-ray scattering (NRIXS) to determine the β-factors of Mössbauer-active elements in minerals (the general moment approach, Polyakov et al. 2005, 2007; Polyakov 2009; Dauphas et al. 2012, 2018). On the other hand, no experimental investigations on the β-factors of Si in minerals have been carried out thus far.

A derivative of the general moment approach is capable of calculating the β-factor from the atomic force constant (Polyakov et al. 2005; Dauphas et al. 2012). If one can determine the atomic force constant of Mössbauer-inactive elements (e.g., Si), it is possible to calculate isotope fractionation β-factors. One way to determine the atomic force constant of Mössbauer-inactive elements is to measure the atomic thermal vibrations in the crystal lattice through single crystal X-ray diffraction. Though X-ray diffraction is hardly sensitive to isotopic effects (Seiler et al. 1984), it proves an effective way to constrain the atomic vibrations in the crystals (Parak and Knapp 1984; Dunitz et al. 1988; Trueblood et al. 1996), whose temperature derivative is directly linked to the atomic force constant (Zaccai 2000; Leu and Sage 2016). In X-ray crystallography, the Debye–Waller factor is the parameter that describes the average atomic displacement around its equilibrium position (Trueblood et al. 1996). Though the Debye–Waller factor is influenced by factors including atomic thermal vibrations, chemical substitutions and local crystalline environment, in the scope of interest to this paper (tetrahedrally coordinated silicon in mantle silicates), the effect of thermal vibration dominates the temperature dependence of the Debye–Waller factor. It is possible to calculate the atomic force constants of Si from the temperature dependence of the Debye–Waller factors through an experiment-based calibration.

Our research is primarily motivated by two issues emerging from pure DFT calculations: I) DFT calculations have suggested that the SiO_4 polyhedral distortion influences the Si isotope fractionation (Méheut and Schauble 2014; Qin et al. 2016), but the effect of polyhedral distortion is controlled by many variables while outliers exist (Méheut and Schauble 2014; Qin et al. 2016). We intend to find one crystallographic parameter to quantify the effect of polyhedral distortion. II) Though the DFT calculations have been successful in resolving the Si isotope fractionation between olivine, albite and pyroxenes, the DFT calculation results that involve silica (SiO_2 polymorph) are not very consistent with mass spectroscopy measurements (Douthitt 1982; Georg 2006; Méheut et al. 2009), and we will examine whether crystal structures affects the isotope fractionation of Si in silica.

In this report, we present an experiment-based calibration of the β-factors of tetrahedrally coordinated silicon (hereafter referred to as ^{IV}Si) in silicate minerals. We first review published general moment approach to determine the β-factor from atomic vibrations and atomic force constants, which are typically measured by NRIXS technique for Mössbauer-active elements. Next, we compile our new experimental and theoretical data together with published data to establish an empirical relationship between the force constants measured from diffraction and used in general moment approach, so that we can apply the force constant measured from diffraction to calculate the β-factor. We then describe the SiO_4 polyhedral distortion with one crystallographic parameter and use the parameter to correct the β-factor. We also compare the isotope fractionation $\ln\alpha_{Si30/28}$ between common minerals measured by mass spectroscopy and determined from our calibration, and discuss the effect of different silica polymorphs. Finally, we discuss the application scope of our calibration and why it is only limited to ^{IV}Si.

Determination of β-factor from the atomic force constant

The isotope fractionation β-factor was first introduced by Bigeleisen and Mayer (1947) and Urey (1947) to study the isotope exchange reactions between different phases. Polyakov et al. (2005) and Dauphas et al. (2012) have proven that, under quasiharmonic approximation, when the maximum phonon energy of pDOS $E_{max} < 2\pi k_B T$ (k_B is the Boltzmann constant), the β-factor can be expanded into a series of the moments of the pDOS (named as the general moment approach):

$$ln\beta_{l/l^*} = \left(\frac{M}{M^*} - 1\right)\left(\frac{m_2^g}{8k_B^2T^2} - \frac{m_4^g}{480k_B^4T^4} + \frac{m_6^g}{20160k_B^6T^6}\right), \quad (1)$$

where M and M^* are the atomic masses of isotopes l and l^*, and the m_i^g is the ith moment of the pDOS $D(E)$, which is defined as:

$$m_i^g = \int_0^\infty E^i D(E)\mathrm{d}E. \quad (2)$$

Atomic force constant ($\langle N\rangle$) is the physical quantity that describes the restoring force that exerts on an atom when the atom is displaced from its equilibrium position in a solid (Leu and Sage 2016). $\langle N\rangle$ is the microscopic counterpart of the macroscopic force constant in Hooke's law. There are two types of $\langle N\rangle$, namely the stiffness and the resilience (Leu and Sage 2016). Stiffness (N_s) (Hu et al. 2013; Leu and Sage 2016) is defined as:

$$N_s = \int M\left(\frac{E}{\hbar}\right)^2 D(E)\mathrm{d}E, \quad (3)$$

where M is the mass of the atom, E is the phonon energy and $D(E)$ is the pDOS. N_s determines the response of an atom to an applied force with all other atoms fixed at their equilibrium positions (Leu and Sage 2016). N_s is more sensitive to the high frequency region of the phonon spectrum, and it primarily probes the nearest-neighbor interactions (Leu and Sage 2016).

The other type of $\langle N\rangle$ is the resilience (N_r), which describes the temperature dependence of the mean square displacement of the atom (Zaccai 2000). N_r is defined as:

$$N_r = \frac{k_B}{\mathrm{d}\langle u^2\rangle/\mathrm{d}T}, \quad (4)$$

where $\langle u^2\rangle$ is the atomic mean square displacement and T is the temperature. At high temperatures where $\frac{E}{k_BT}$ is sufficiently small over the whole range of phonon spectrum, N_r is approximated by the following equation (Hu et al. 2013):

$$N_r = \frac{M}{\int(\frac{\hbar}{E})^2 D(E)\mathrm{d}E} \quad (5)$$

N_r determines the response of an atom to an applied force with the surrounding atoms free to respond and the center of mass fixed (Leu and Sage 2016). Compared to N_s, N_r is sensitive to the low frequency region of the phonon spectrum (Hu et al. 2013; Leu and Sage 2016).

Based on Eqs. 3 and 5, the N_s and N_r are related through the pDOS ($D(E)$). Though the phonon spectrum can be measured experimentally though inelastic X-ray/neutron scattering, in most cases, the measurements on the pDOS of Mössbauer inactive elements are too complicated to be practically carried out. Therefore, many researchers use simplified physical models to describe the phonon spectrum in solids. Those physical models usually have only a few key parameters that are directly linked to physical measurements. The Debye model is the most commonly used model to describe the phonon density of states in minerals (Leu and Sage 2016; Zhang et al. 2021). The phonon spectrum in the Debye model has the following formula:

$$D(E) = \begin{cases} \frac{3E^2}{(k_B\theta_D)^3} & (E \le k_B\theta_D), \\ 0 & (E > k_B\theta_D), \end{cases} \quad (6)$$

where the parameter θ_D is the material-specific Debye temperature (Singwi and Sjölander 1960; Leu and Sage 2016). If the pDOS of the element of interest follows the Debye model, we have (Leu and Sage 2016):

$$N_s = \frac{9}{5}N_r. \tag{7}$$

Under the assumption that the pDOS follows the Debye model, so that m_i^g is explicitly expressed as a function of N_s (Dauphas et al. 2018), Eq. 1 is further reduced to a polynomial series of N_s:

$$ln\beta_{I/I^*} = \left(\frac{\hbar^2}{8k_B^2}\frac{N_s}{T^2} - \frac{5\hbar^4}{2016k_B^4 M}\frac{N_s^2}{T^4} + \frac{25\hbar^6}{326592k_B^6 M^2}\frac{N_s^3}{T^6}\right)\left(\frac{1}{M^*} - \frac{1}{M}\right). \tag{8}$$

Constrain the atomic force constant from X-ray diffraction

Debye–Waller factor and atomic vibrations

In 1913, Peter Debye found that the thermal vibration of atoms in solids would influence the intensity of X-ray diffraction signal (Debye 1913). Debye's finding later led to the Debye–Waller factor, which is defined as (Trueblood et al. 1996):

$$T(\mathbf{h}) = \int p(\mathbf{u})\exp(2\pi i\mathbf{h}\cdot\mathbf{u})d^3\mathbf{u}, \tag{9}$$

where $\mathbf{h}$ is the diffraction vector obeying the diffraction condition, $p(\mathbf{u})$ is the probability density function of the atom displaced by the vector $\mathbf{u}$ from its equilibrium position in the unit cell. If one assumes that: (I) the static atomic electron density has spherical symmetry, and (II) the probability density function of the atomic displacement is Gaussian, Eq. 9 transforms to (Trueblood et al. 1996; Kuhs 2013):

$$T(\mathbf{h}) = e^{-2\pi^2\langle(\mathbf{h}\cdot\mathbf{u})^2\rangle}. \tag{10}$$

If one further assumes that the atomic displacement is isotropic, Eq. 10 then simplifies to (Trueblood et al. 1996; Kuhs 2013):

$$T(|\mathbf{h}|) = e^{-2\pi^2\langle u^2\rangle(sin^2\theta)/\lambda^2}, \tag{11}$$

where $\langle u^2\rangle$ is the atomic mean-square displacement, θ is the diffraction angle, and λ is the wavelength of the X-ray. The Debye–Waller factor is an experimental measurable quantity and is proportional to $\bar{I}/\Sigma f^2$, where $\bar{I}$ is the averaged peak intensity and Σf^2 is the sum of atomic scattering factors (Brown et al. 2006; Coppens 2010). The isotropic Debye–Waller factor $T(|\mathbf{h}|)$ is a function of both θ and λ. To remove the dependence on θ and λ, crystallographers prefers the temperature B-factor to describe the atomic thermal vibrations. The B-factor is calculated by fitting the slope of $ln(\bar{I}/\Sigma f^2)$ as a function of squared resolution $(sin^2\theta/\lambda^2)$ (Wilson 1949). The relationship between B-factor and $\langle u^2\rangle$ is defined by the following equation (Trueblood et al. 1996):

$$\langle u^2\rangle = \frac{B}{8\pi^2}. \tag{12}$$

The Debye–Waller factor is very similar to the Lamb–Mössbauer factor (f_{LM}) that is commonly measured by conventional Mössbauer spectroscopy or nuclear resonant scattering (Sturhahn and Chumakov 1999; Hu et al. 2013). f_{LM} is defined as the recoilless fraction of the total Mössbauer absorption spectrum (Sturhahn and Chumakov 1999), and it is related to $\langle u^2\rangle$ through the following equation (Hu et al. 2013):

$$f_{LM} = \exp(-k^2\langle u^2\rangle), \tag{13}$$

where k is the wavenumber of the Mössbauer resonant X-ray photon. $T(|\mathbf{h}|)$ is very similar and closely related to f_{LM}, but they are intrinsically different. f_{LM} is related to the photon interaction with nuclei, and has a slow scattering time scale (usually in the order of 10–100 ns); whereas $T(|\mathbf{h}|)$ comes from electronic charge scattering of photon which is a nearly instantaneous process (Sturhahn and Chumakov 1999).

Difference and relationship between resiliences measured by different techniques

Based on the discussions in Sects. "Determination of β-factor from the atomic force constant" and "Debye–Waller factor and atomic vibrations", there are at least two methods to constrain the resilience of an isotope in minerals:

1. First determine $\langle u^2\rangle$ as a function of temperature from the Debye–Waller factor derived from X-ray diffraction, and then calculate the resilience using Eq. 4 (hereafter referred as the N_{rD});
2. First determine the pDOS ($D(E)$) using theoretical calculation or nuclear resonant inelastic X-ray scattering (if the isotope is Mössbauer active), and then calculate the resilience from Eq. 5. Equivalently, for Mössbauer active isotopes, one can measure the temperature dependence of f_{LM}, calculate $\langle u^2\rangle$ as a function of temperature using Eq. 13, and then calculate the resilience from Eq. 4 (Hu et al. (2013), hereafter referred as the N_{rM}).

N_{rD} and N_{rM} are different physical quantities. N_{rD} reflects the temperature dependence of the mean-square displacement of electron density in the material (referred to as $\langle u_e^2\rangle$), whereas N_{rM} reflects the temperature dependence of the mean-square displacement of nuclei in the material (referred to as $\langle u_n^2\rangle$) (Parak et al. 1988; Dunitz et al. 1988). $\langle u_n^2\rangle$ directly reflects the behavior of the phonon spectrum, because the majority of the atomic mass is contributed by the nuclei, and the vibrational frequency of the phonon depends on the atomic mass. On the other hand, the atomic electron cloud is not rigid, and the electron density could be distorted during thermal vibration (Dunitz et al. 1988) (Fig. 1C). As a result, $\langle u_e^2 \rangle$ is different from $\langle u_n^2 \rangle$, and doesn't directly reflect the phonon behavior. It is necessary to calibrate N_{rD} against N_{rM} if one would like to use N_{rD} to study vibrational behavior in the sample. Besides, $\langle u_e^2 \rangle$ has a static component compared to $\langle u_n^2 \rangle$ (Parak and Knapp 1984), but this static component is temperature-independent (Parak et al. 1987; Nakatsuka et al. 2011) and does not contribute to the determination of N_{rD}.

To our knowledge, no study has quantified the relationship between N_{rD} and N_{rM} across different materials, so an *a priori* model is needed to establish such a relationship. We assume that the temperature dependence of $\langle u_n^2 \rangle$ and the temperature dependence of $\langle u_n^2 \rangle$ has a linear relationship:

$$\frac{\mathrm{d}\langle u_n^2 \rangle}{dT} = B' \times \frac{\mathrm{d}\langle u_e^2 \rangle}{\mathrm{d}T} + A', \tag{14}$$

where B' and A' are fitting coefficients. Considering the fact that several recent studies on isotope fractionation prefer to use stiffness from pDOS (referred to as N_{sM}) to calculate the β-factor, we would like to involve N_{sM} into our calculation. If we further assume that the pDOS follows quasiharmonic Debye model so that Eq. 7 is valid, then from Eqs. 14 and 7 we get:

$$C_{sM}^{rD} \equiv \frac{N_{rD}}{N_{sM}} = \frac{5A'}{9k_B} \times N_{rD} + \frac{5B'}{9} \equiv A \times N_{rD} + B, \tag{15}$$

where A ($= 5A'/9k_B$, A' comes from Eq. 14) and B ($= 5B'/9$, B' comes from Eq. 14) are fitting coefficients. Eq. 15 suggests that the ratio between N_{rD} and N_{sM} (hereafter referred to as C_{sM}^{rD}) is a linear function of N_{rD}. Equation 15 requires our *a priori* model between N_{rD} and N_{rM} (Eq. 14), and its validity will be examined against experimental data in "Calibration of the resilience–stiffness relationship in ^{IV}Si" section.

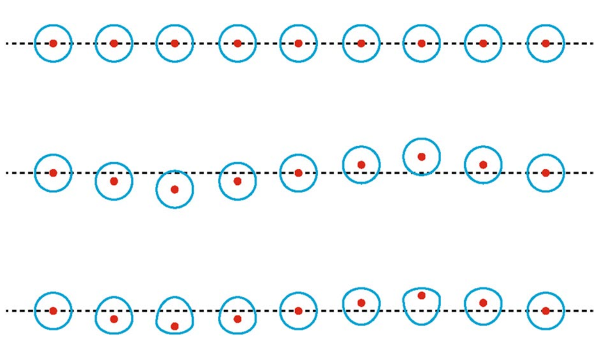

Fig. 1 Illustration demonstrating the difference between $\langle u_n^2 \rangle$ and $\langle u_e^2 \rangle$. Red dot: nuclei; cyan circle: electron cloud; black dashed line: equilibrium position. Static disorder is neglected in this illustration. A No thermal vibration. All atoms are fixed at equilibrium position. B Rigid atoms. Electron cloud moves simultaneously with nuclei during thermal vibration, and in this case $\langle u_n^2 \rangle = \langle u_e^2 \rangle$. C Real atoms. Electron cloud moves and distorts during thermal vibration, and in this case $\langle u_n^2 \rangle \neq \langle u_e^2 \rangle$

Single crystal X-ray diffraction experiments

While compiling N_{rD} from published single crystal diffraction data, we have noticed that X-ray diffraction data on orthoenstatite ($Mg_2\,Si_2\,O_6$) and α-quartz (SiO_2) are sparse compared to other common minerals (Table 3). To improve the statistics of N_{rD} measurement, we have taken single crystal X-ray diffraction on synthetic orthoenstatite and synthetic α-quartz crystals. Fragments of orthoenstatite and α-quartz crystals with a size of $\sim 80 \times 80{\times}150\ \mu\,\mathrm{m}^3$ were mounted into a fused silica capillary with 100 μm inner diameter. High temperature single crystal X-ray diffraction experiments were carried out at the experimental station 13-BM-C of the Advanced Photon Source, Argonne National Laboratory (Zhang et al. 2017). The X-ray beam was monochromated with a silicon 311 crystal to a wavelength of 0.434 Å, with 1 eV bandwidth. A Kirkpatrick–Baez mirror system was used to obtain a vertical × horizontal focus spot size of 18 μm × 12 μm measured at full width-half maximum. A Pilatus3 1M photon counting area detector with 1 mm silicon sensor (Dectris) was placed about 190 mm away from the sample, and LaB_6 powder was used to calibrate the distance and tilting of the detector. The sample was placed at the rotation center of the diffractometer, and was aligned with an optical microscope. In each measurement, the sample rotated along the ϕ-axis of the diffractometer. The ϕ-rotation covered a range of 340°, and was segmented into 340 images. The exposure time of each images was 0.5 s. The sample temperature was controlled by helium flow heated with a tungsten heater up to 600 K, and a K-type thermal couple was placed near the sample to read the temperature. With an automatic temperature feedback loop, the fluctuation of temperature during each measurement was smaller than 1 K. The maximum deviation between the temperature determined by the thermal couple and the temperature determined from the published thermal expansion coefficient of orthoenstatite and α-quartz is 2% (Kihara 1990; Jackson et al. 2003). All measurements were carried out at 1 bar pressure.

The diffraction images were analyzed using the APEX3 software (Bruker). Diffraction peaks were harvested from the images with APEX3 software, and changes in the sample illuminated volume and the absorption effects were corrected using the SADABS software. Corrected peak intensities were used to refine the crystal structures with SHELXL software, facilitated by Olex2 general user interface (Dolomanov et al. 2009; Sheldrick 2008). We used isotropic Debye–Waller factor for all ions in the refinement, and all structural sites were assumed to be fully occupied by Mg^{2+}, Si^{4+} or O^{2-} ions. Refinements with anisotropic Debye–Waller factor of Si^{4+} were tested (Watkin 2008), and the anisotropic refinement gave the same equivalent isotropic Debye–Waller factor of Si^{4+} as isotropic refinement within the experimental error, so we report Debye–Waller factors of Si^{4+} from isotropic refinement in this paper. Within our investigated temperature range, the orthoenstatite crystal maintained the orthorhombic P*bca* space group, while the α-quartz crystal maintained the trigonal $P3_221$ space group. Unit cell parameters, fractional atomic positions, and $\langle u^2 \rangle$ of each atom in α-quartz and orthoenstatite measured at different temperatures are listed in Tables 1 and 2, respectively. The $\langle u^2 \rangle$ of Si^{4+} of orthoenstatite and α-quartz are illustrated in Fig. 2.

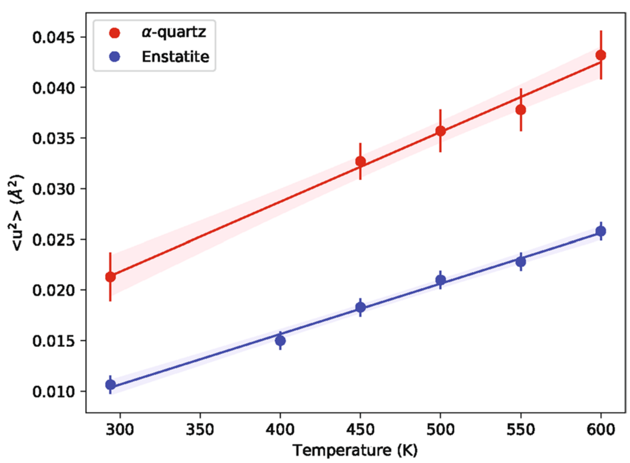

Fig. 2 $\langle u_e^2 \rangle$ of silicon in α-quartz (red symbols) and orthoenstatite (blue symbols) measured at different temperatures from the single crystal X-ray diffraction of this study. Straight lines are the linear regressions of the measured data. Shaded regions indicate the 1-σ confidence interval of the linear regression. The slope of the linear regression is used to calculate the N_rD using Eq. 4

Density functional theory calculation

To benchmark the N_{sM} that we derived from published β-factors, we have carried out density functional theory calculation to calculate the Si partial phonon DOS in orthoenstatite and α-quartz. Energy and nuclei forces are evaluated with Perdew–Burke–Ernzerhof (PBE) exchange-correlation functional (Perdew et al. 1996). The calculations were performed by Quantum ESPRESSO (Giannozzi et al. 2009, 2017) with plane wave basis and Projector-augmented wave (PAW) (Blöchl 1994) pseudopotentials from Pslibrary (Corso 2014). The kinetic energy cutoff for wavefunctions was set to 50 Ry while the kinetic energy cutoff for charge density was et to 360 Ry for both systems. Structure and unit cell parameters were optmized before phonon calculation for both systems.

The pDOS was calculated by Phonopy package (Togo and Tanaka 2015) (Fig. 3). The crystal structures of orthoenstatite and α-quartz at ambient P–T condition determined from single crystal X-ray diffraction was used as input. Force constants were evaluated with finite finite displacement approaches with atomic displacement distance 0.01 Å. $2 \times 2 \times 2$ supercell of the unit cell was used for quartz and $1 \times 1 \times 2$ supercell of the unit cell was used for for orthoenstatite. A $2 \times 2 \times 2$ k-point sampling was used in all supercell calculations of quartz while a $1 \times 2 \times 2$ k-point sampling was used in all supercell calculations of orthoenstatite. The size of supercell and the number of k points were tested to ensure convergence.

Calibration of the resilience–stiffness relationship in ^{IV}Si

We determined the N_{rD} and N_{sM} of different polymorphs of SiO_2 silica, albite, olivine, diopside, orthoenstatite and pyrope garnet with existing single crystal diffraction data

Table 1 Unit cell parameters, fractional atomic position, and $\langle u^2 \rangle$ of each atom in α-quartz determined by single crystal diffraction in this study

T	(K)	295	450	500	550	600
a	(Å)	4.9136(7)	4.9275(7)	4.9322(7)	4.9374(6)	4.9444(6)
c	(Å)	5.403(1)	5.411(1)	5.415(1)	5.419(1)	5.422(1)
Volume	(AA^3)	112.98(6)	113.77(6)	114.07(6)	114.40(5)	114.79(5)
Si	x	0.4698(4)	0.4721(3)	0.5272(4)	0.4738(4)	0.5252(4)
	y	1	1	1	1	1
	z	0.6667	0.6667	0.6667	0.6667	0.6667
$\langle u^2 \rangle$	(AA^2)	0.021(2)	0.033(2)	0.036(2)	0.038(2)	0.043(2)
O	x	0.1461(8)	0.1511(8)	0.2614(9)	0.155(1)	0.258(1)
	y	0.7331(7)	0.7368(8)	0.8471(9)	0.740(1)	0.842(1)
	z	0.5472(6)	0.5437(6)	0.4572(6)	0.5412(7)	0.4604(8)
$\langle u^2 \rangle$	(AA^2)	0.032(3)	0.058(3)	0.065(3)	0.071(4)	0.081(4)

α-quartz has a trigonal crystal structure (lattice parameter $a = b, \alpha = \beta = 90°, \gamma = 120°$)

Table 2 Unit cell parameters, fractional atomic position and $\langle u^2 \rangle$ of each atom in orthoenstatite determined by single crystal diffraction in this study

T	(K)	294	400	450	500	550	600
a	(Å)	18.250(2)	18.267(2)	18.275(2)	18.280(2)	18.289(2)	18.298(2)
b	(Å)	8.8244(9)	8.8380(9)	8.8441(9)	8.850(1)	8.8564(9)	8.8628(9)
c	(Å)	5.1862(5)	5.1924(5)	5.1953(5)	5.1979(5)	5.2013(5)	5.2044(5)
Volume	(AA^3)	835.2(2)	838.3(2)	839.7(2)	840.9(2)	842.5(2)	844.0(2)
Mg1	x	0.37580(4)	0.37572(4)	0.37574(5)	0.37573(5)	0.37564(5)	0.37562(6)
	y	0.65387(8)	0.65361(9)	0.6535(1)	0.6533(1)	0.6531(1)	0.653(1)
	z	0.8658(1)	0.8669(2)	0.8675(2)	0.8682(2)	0.8688(2)	0.8694(2)
$\langle u^2 \rangle$	(AA^2)	0.0138(9)	0.0198(9)	0.0237(9)	0.0267(9)	0.0294(9)	0.0339(9)
Mg2	x	0.37685(4)	0.37678(5)	0.37683(5)	0.37682(5)	0.37673(5)	0.37677(6)
	y	0.48663(9)	0.4867(1)	0.4867(1)	0.4868(1)	0.4868(1)	0.4868(1)
	z	0.3588(1)	0.3600(2)	0.3606(2)	0.3613(2)	0.3619(2)	0.3627(2)
$\langle u^2 \rangle$	(AA^2)	0.0198(9)	0.0279(9)	0.0330(9)	0.0372(9)	0.0405(9)	0.0462(9)
SiA	x	0.27165(4)	0.27167(4)	0.27165(4)	0.27165(4)	0.27166(4)	0.27170(5)
	y	0.34160(7)	0.34147(7)	0.34137(8)	0.34131(8)	0.34126(8)	0.34125(9)
	z	0.0501(1)	0.0507(1)	0.0512(1)	0.0516(1)	0.0519(1)	0.0523(1)
$\langle u^2 \rangle$	(AA^2)	0.0105(9)	0.0150(9)	0.0183(9)	0.0210(9)	0.0228(9)	0.0258(9)
SiB	x	0.47363(3)	0.47378(4)	0.47379(4)	0.47390(4)	0.47396(4)	0.47403(5)
	y	0.33748(6)	0.33750(7)	0.33754(7)	0.33754(8)	0.33757(8)	0.33760(9)
	z	0.7984(1)	0.7977(1)	0.7975(1)	0.7972(1)	0.7967(1)	0.7963(2)
$\langle u^2 \rangle$	(AA^2)	0.0108(9)	0.0150(9)	0.0183(9)	0.0210(9)	0.0228(9)	0.0258(9)
O1A	x	0.18354(9)	0.1837(1)	0.1837(1)	0.1839(1)	0.1839(1)	0.184(1)
	y	0.3401(2)	0.3400(2)	0.3401(2)	0.3399(2)	0.3401(2)	0.3400(2)
	z	0.0356(3)	0.0369(3)	0.0373(3)	0.0381(3)	0.0391(3)	0.0397(4)
$\langle u^2 \rangle$	(AA^2)	0.017(1)	0.023(1)	0.027(2)	0.031(2)	0.032(2)	0.036(2)
O1B	x	0.31088(8)	0.31092(9)	0.31098(9)	0.3110(1)	0.3110(1)	0.3110(1)
	y	0.5022(2)	0.502(2)	0.5016(2)	0.5016(2)	0.5013(2)	0.5009(3)
	z	0.0434(3)	0.0448(3)	0.0456(3)	0.0464(3)	0.0470(3)	0.0477(4)
$\langle u^2 \rangle$	(AA^2)	0.019(1)	0.026(1)	0.030(2)	0.034(2)	0.038(2)	0.042(2)
O2A	x	0.30313(8)	0.30314(9)	0.3030(1)	0.3031(1)	0.3030(1)	0.3030(1)
	y	0.2233(2)	0.2237(2)	0.2241(2)	0.2245(2)	0.2245(2)	0.2249(3)
	z	0.8312(3)	0.8313(3)	0.8315(3)	0.8315(3)	0.8315(3)	0.8318(4)
$\langle u^2 \rangle$	(AA^2)	0.018(1)	0.024(1)	0.028(2)	0.032(2)	0.034(2)	0.040(2)
O2B	x	0.56224(9)	0.5622(1)	0.5623(1)	0.5622(1)	0.5622(1)	0.5624(1)
	y	0.3402(2)	0.3403(2)	0.3404(2)	0.3406(2)	0.3405(2)	0.3406(2)
	z	0.8002(3)	0.7995(3)	0.7991(3)	0.7987(3)	0.7981(3)	0.7978(4)
$\langle u^2 \rangle$	(AA^2)	0.017(1)	0.022(1)	0.026(2)	0.029(2)	0.032(2)	0.035(2)
O3A	x	0.43280(8)	0.43279(9)	0.4329(1)	0.4329(1)	0.4328(1)	0.4329(1)
	y	0.4828(2)	0.4828(2)	0.4828(2)	0.4828(2)	0.4827(2)	0.4830(2)
	z	0.6896(3)	0.6902(3)	0.6903(3)	0.6906(3)	0.6910(4)	0.6911(4)
$\langle u^2 \rangle$	(AA^2)	0.020(1)	0.027(1)	0.031(1)	0.035(2)	0.038(2)	0.042(2)
O3B	x	0.44760(9)	0.44769(9)	0.4477(1)	0.4478(1)	0.448(1)	0.448(1)
	y	0.1955(2)	0.1965(2)	0.1969(2)	0.1972(2)	0.1976(2)	0.1980(2)
	z	0.6037(3)	0.6020(3)	0.6016(3)	0.6006(3)	0.6001(3)	0.5993(4)
$\langle u^2 \rangle$	(AA^2)	0.018(1)	0.025(1)	0.028(1)	0.032(2)	0.034(2)	0.038(2)

Orthoenstatite has a orthorhombic crystal structure (lattice parameter $\alpha = \beta = \gamma = 90°$)

and theoretical DFT calculations published in the past 48 years (Table 3). The N_{rD} is fitted from the temperature dependence of $\langle u^2 \rangle$ using Eq. 4. Most theoretical studies did not directly report the N_{sM} of each mineral, and instead,

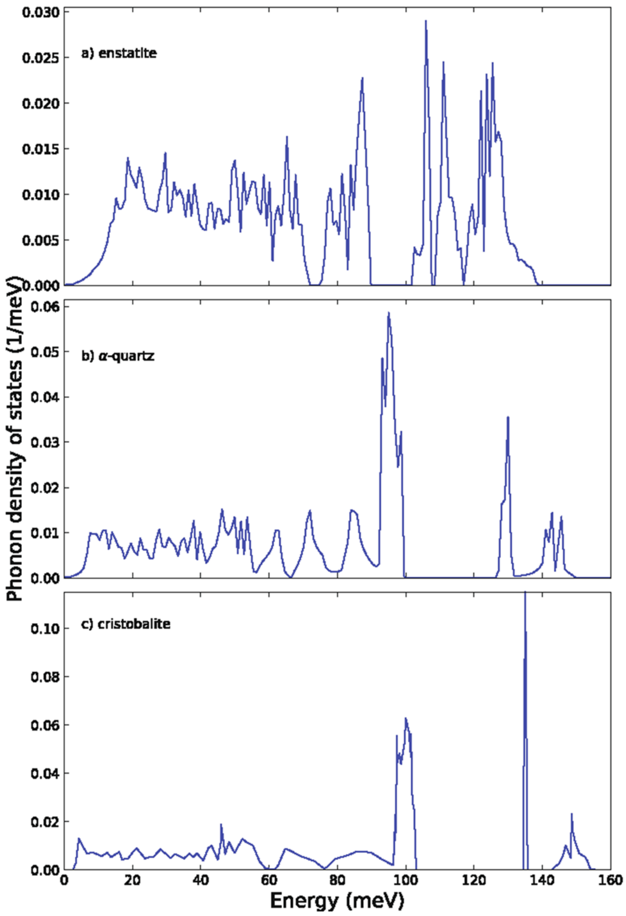

Fig. 3 The pDOS of ^{IV}Si in select minerals. a) orthoenstatite (this study); b) α-quartz (this study); c) cristobalite (digitized from Wehinger et al. (2015))

the authors usually expanded the temperature dependence of the lnβ of each element as a polynomial function of $x = 10^6/T^2$. Since the lnβ is well approximated as a function of temperature by Eq. 8 (Dauphas et al. 2018), the N_{sM} of ^{IV}Si of each mineral is fitted from the temperature dependence of lnβ. As different studies use different polynomials of x to expand lnβ, for the sake of consistency, only the linear term is used to fit the N_{sM}. Minerals like orthoenstatite and albite have more than one ^{IV}Si sites due to crystal symmetry. The N_{rD} of each ^{IV}Si site is calculated individually from the temperature dependence of the Debye–Waller factor of each site, and the N_{rD} of the mineral is reported as the arithmetic average of the N_{rD}s of all ^{IV}Si sites.

We explored the relationship between N_{rD} and C_{sM}^{rD} in light of Eq. 15, and found that they follow a very good linear trend ($R^2 = 0.9992$). The *a priori* model (Eq. 14) used to construct Eq. 15 seems justified for ^{IV}Si. Our best-fit model gives the coefficient $A = 1.63(6) \times 10^{-3}$ m/N, and $B = -5.20(2) \times 10^{-3}$ (Fig. 4). By combining Eqs. 8 and 15, one can calculate the N_{sM} of ^{IV}Si from the N_{rD}, and then calculate the ln$\beta_{Si30/28}$ factor for each mineral at different temperatures from the N_{sM}. We name our approach to calculate the ln$\beta_{Si30/28}$ factor as the *force constants* approach, as the two force constants (resilience N_{rD} and stiffness N_{sM}) are the key parameters that link the crystallographic Debye–Waller factor to the isotope fractionation β-factor.

Determination of the uncertainty

The aggregate error of the averaged force constants (N_{rD} and N_{sM}) is determined by two components: the first component is the error of each individual force constant measurement (which indicates the precision of each measurement), and the second component is the scattering of force constant values from different measurements. Given the condition that each measurement of the force constant on a specific mineral is independent to each other, the aggregate error of the averaged force constant on the specific mineral is determined by the pooled variance of all measurements using the following equation (O'Neill 2014):

$$\sigma_N = \sqrt{\frac{\sum_{i=1}^{M}(N_i^2 + \sigma_{N_i}^2)}{M} - \frac{\left(\sum_{i=1}^{M} N_i\right)^2}{M^2}}, \quad (16)$$

where N_i is the force constant (N_{rD} or N_{sM}) from each individual measurement, σ_{N_i} is the error of each individual force constant measurement, M is the total number of force constant measurements for the specific mineral, and σ_N is the aggregate error of the averaged force constant. Once the error of the average resilience ($\sigma_{N_{rD}}$) and the error of the average stiffness ($\sigma_{N_{sM}}$) are determined from Eq. 16, the error of C_{sM}^{rD} is determined from the error propagation formula:

$$\sigma_{C_{sM}^{rD}} = C_{sM}^{rD} \times \sqrt{\left(\frac{\sigma_{N_{rD}}}{N_{rD}}\right)^2 + \left(\frac{\sigma_{N_{sM}}}{N_{sM}}\right)^2} \quad (17)$$

The uncertainty of the C_{sM}^{rD} calibration is evaluated by the prediction interval of Eq. 15 (Fig. 4). The errors of N_{rD} and C_{sM}^{rD} have the feature that the scattering of data from different studies is larger than the precision of each individual measurement (Table 3), which leads to the issue that in Fig. 4, data point that is better covered by previous studies (e.g., olivine) have an error bar that is larger than data point that is less covered by previous studies. So the small error bar in certain points in Fig. 4 does not necessarily indicate that the uncertainties of these minerals are small, but an indication that their sample coverage is poor. The error bar of olivine, which is the best-sampled mineral by previous studies,

Table 3 N_{rD} and N_{sM} of ^{IV}Si calculated from published data and this study

Mineral	N_{rD} (N/m)		N_{sM} (N/m)	
Olivine	35(2)	Smyth and Hazen (1973)	652.6	Méheut and Schauble (2014)
	42(3)	Hazen (1976)	645.2	Huang et al. (2014)
	35.4(9)	Bo10, Heinemann et al. (2006)	715.5	Wu et al. (2015)
	29(3)	Bo2, Heinemann et al. (2006)	738.7	Qin et al. (2016)
	38(1)	Heinemann et al. (2007)		
Orthoenstatite[a]	31(3)	Yang and Ghose (1995)	645.9	Méheut and Schauble (2014)
	28(2)	This study	667.8	Huang et al. (2014)
			731.6	Qin et al. (2016)
			687.3	This study[c]
Diopside	32(2)	Cameron et al. (1973)	649.6	Huang et al. (2014)
			723.1	Qin et al. (2016)
α−quartz	17.6(5)	Kihara (1990)	688.4	Méheut and Schauble (2014)
	20(2)	This study	776.3	Qin et al. (2016)
			708.0	This study[c]
Albite[b]	22.5(4)	Prewitt et al. (1976)	682.5	Méheut and Schauble (2014)
	22.8(8)	Winter et al. (1977)	771.8	Qin et al. (2016)
Pyrope	58(4)	Meagher (1975)	634.6	Méheut and Schauble (2014)
	54.2(6)	Pavese et al. (1995)	661.0	Huang et al. (2014)
	55.4(6)	Nakatsuka et al. (2011)		
Cristobalite	13.5(3)	Peacor (1973)	791.5	Wehinger et al. (2015)[c]
β−quartz	28(3)	Kihara (1990)	-	-

[a]: average of SiA and SiB sites. [b]: average of all tetrahedral sites. [c]: stiffness calculated from pDOS using Eq. 3

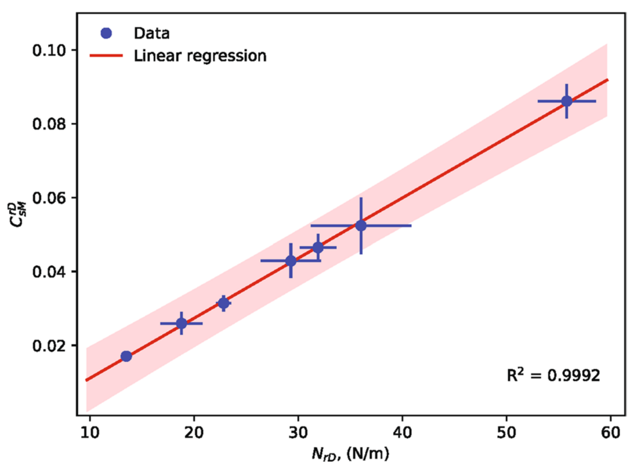

Fig. 4 Best linear regression of the resilience–stiffness ratio C_{sM}^{rD} as a function of the resilience N_{rD} (Eq. 15) for ^{IV}Si in crust and mantle minerals. Red shaded region indicate the uncertainty of the linear regression constrained by Eq. 18. R^2 of the linear regression is 0.9992

should be representative of this method. Given a determined N_{rD}, the uncertainty of the corresponding C_{sM}^{rD} is defined by the prediction interval of the linear regression Eq. 15:

$$\mathrm{d}C_{sM}^{rD} = t_{M-2}s_Y\sqrt{1+\frac{1}{n}+\frac{(N_{rD}-\overline{N_{rDi}})^2}{\sum_{i=1}^{M}(N_{rDi}-\overline{N_{rDi}})^2}},$$
$$s_Y=\sqrt{\frac{\sum_{i=1}^{M}(C_{sMi}^{rD}-AN_{rDi}-B)^2}{n-2}}, \tag{18}$$

where $\mathrm{d}C_{sM}^{rD}$ is the prediction interval of the calibration curve (Eq. 15), C_{sMi}^{rD} and N_{rDi} are the C_{sM}^{rD} and N_{rD} for the ith mineral, $\overline{N_{rDi}}$ is the mean resilience of all minerals covered by this study, M is the total number of minerals, t_{M-2} is a coefficient related to the Student's t distribution on $M-2$ degrees of freedom and the confidence level. In our case, we choose a t_{M-2} that makes the dC_{sM}^{rD} of olivine same as its error bar, because olivine has the best sample coverage. Among the silicates investigated in this study, the range of dC_{sM}^{rD} is around 0.0075 (Fig. 4). This dC_{sM}^{rD} value is used to estimate the uncertainty in isotope fractionation α factor between minerals in the following section.

Discussion

Correction of N_s based on crystal distortion

The size and shape of SiO_4 tetrahedron within the mineral has a strong effect on the Si isotope fractionation. It is already known that the SiO_4 tetrahedral volume and the average Si–O bond length play a primary role in the Si isotope fractionation (Méheut and Schauble 2014; Qin et al. 2016), as the SiO_4 tetrahedral volume and Si–O bond length determine the Si–O bond strength and hence influences the force constant (Leu and Sage 2016). Schauble (2004) suggests that silicates with shorter Si–O bonds in general show heavier silicon isotopic compositions, because shorter Si–O bonds are expected to be stronger. Linear relationships between the isotope fractionation β-factor and the SiO_4 tetrahedral volume/average Si–O bond length hold in general (Méheut and Schauble 2014; Qin et al. 2016), while outliers exist. Méheut and Schauble (2014) find that in phyllosilicates, Si–O bonds that are perpendicular to the tetrahedra layers ($Si\text{-}O_{\perp}$) have a negative correlation with Si–O bonds that are parallel to the tetrahedra layers ($Si\text{-}O_{\parallel}$). Méheut and Schauble (2014) also suggests that the phyllosilicate with a shorter $Si\text{-}O_{\perp}$ bond length tends to have a longer average Si-O bond length, and hence a weaker Si–O bond strength. Qin et al. (2016) demonstrates a correlation between the Si isotopic fractionation and the average Si–O bond length and the SiO_4 tetrahedral volume, with an obvious outlier of zircon. In the case of zircon, Qin et al. (2016) indicates that the repulsion between the Zr^{4+} and Si^{4+} leads to the large distortion of the SiO_4 tetrahedra, and further lead to the deviation of zircon from the relationship between Si isotopic fractionation and Si–O bond length/SiO_4 tetrahedral volume established in other silicates. Besides the first order effect on the Si isotopic fractionation from the SiO_4 tetrahedral volume/average Si–O bond length, secondary effect from SiO_4 tetrahedral distortions should also be considered.

A crystallographic parameter named the effective coordination number (ECoN) is a good parameter to characterize the polyhedral distortions within the mineral crystal (Hoppe 1979). ECoN is defined from the following equations (Hoppe 1979; Hoppe et al. 1989; Momma and Izumi 2011):

$$\begin{aligned} \mathrm{ECoN} &= \sum_i exp\left[1 - \left(\frac{l_i}{l_{av}}\right)^6\right] \\ l_{av} &= \frac{\sum_i l_i exp\left[1 - (l_i/l_{min})^6\right]}{\sum_i exp\left[1 - (l_i/l_{min})^6\right]}, \end{aligned} \quad (19)$$

where l_i is the ith bond length of the polyhedron, l_{min} is the smallest bond length in the polyhedron, and l_{av} is a weighted average bond length. ECoN is a geometric parameter and depends on the shape of the polyhedron of interest, and reflects the deviation of the effective charge of the central cation in the polyhedron from the formal charge (Hoppe et al. 1989; Nespolo et al. 1999). For SiO_4 tetrahedron, the relationship between ECoN, the effective charge and the real charge of the Si^{4+} central cation is as follows (Hoppe et al. 1989; Momma and Izumi 2011):

$$\frac{\text{Effective charge}}{\text{Real charge}} = \frac{\mathrm{ECoN}}{4}. \quad (20)$$

Table 4 ECoN of SiO_4 tetrahedron in each mineral

Mineral	ECoN	Reference
Olivine	3.9903	Smyth and Hazen (1973)
	3.9906	Hazen (1976)
	3.9917	Bo10, Heinemann et al. (2006)
	3.9902	Bo2, Heinemann et al. (2006)
	3.9902	Heinemann et al. (2007)
Enstatite[a]	3.9500	Yang and Ghose (1995)
	3.9251	This study
Diopside	3.8936	Cameron et al. (1973)
α–quartz	3.9991	Kihara (1990)
	3.9997	This study
Albite[b]	3.9963	Prewitt et al. (1976)
	3.9860	Winter et al. (1977)
Pyrope	4	Symmetry[c]
Cristobalite	3.9998	Peacor (1973)
β–quartz	4	Symmetry[c]

[a] Average of SiA and SiB sites. [b] Average of all tetrahedral sites. [c] ECoN is fixed to 4 due to the constraints of crystal symmetry

The ECoN of SiO_4 tetrahedron in each mineral is listed in Table 4. The bond strength is expected to be proportional to the oxidation state of the central cation in the tetrahedron (Pauling 1929). Though all the ^{IV}Si cations in the silicate minerals explored by this study have an nominal oxidation state of +4, their effective oxidation state is proportional to the ECoN of ^{IV}Si (Eq. 20), so their bond strength is also proportional to ECoN. In our model, we correct the stiffness that is used to calculate the isotope fractionation (N_{sMC}) from the stiffness calculated from Eq. 15 (N_{sM}) with the following equation:

$$N_{sMC} = N_{sM} \times \frac{\mathrm{ECoN}}{4}. \quad (21)$$

The correction based on ECoN has a strong effect on pyroxenes such as orthoenstatite and diopside, which have smaller ECoN than other minerals explored in this study (Table 4). Without the correction, Eq. 15 would overestimate the N_{sM} by ~ 2% (about 14 N/m) in pyroxene. The correction is important in determining the Si isotope fractionation between pyroxenes and other minerals.

Comparison with mass spectrometry studies and DFT calculations

Mass spectrometry experiments provide the α-factor between two phases, which is the ratio between their corresponding β-factors. In many papers, the β-factor is calculated in its logarithmic form (lnβ), and then the corresponding α-factor in logarithmic form is calculated with the following equation: $\ln\alpha_{A-B} = \ln\beta_A - \ln\beta_B$. In our *force constants* approach, we calculate the $\ln\alpha_{Si30/28}$ between minerals A and B using the following protocol. First, we calculate the averaged N_{rD} of minerals A and B from the temperature dependence of the Debye–Waller factor of ^{IV}Si from all available diffraction studies (Table 3). Then, the C_{sM}^{rD} is calculated from the averaged N_{rD} using Eq. 15, and N_{sM} is calculated from N_{rD} and C_{sM}^{rD} using Eq. 15. The N_{sM} is then corrected with the ECoN of the SiO_4 tetrahedron using Eq. 21. Finally, the corrected N_{sMC} is used to calculate the isotope fractionation $\ln\beta_{Si30/28}$ at various temperatures using Eq. 8, and the $\ln\beta_{Si30/28}$ of mineral A is subtracted with the $\ln\beta_{Si30/28}$ of mineral B to get the $\ln\alpha_{Si30/28}$ between A and B. The uncertainty of the $\ln\alpha_{Si30/28}$ is estimated from the averaged uncertainty of C_{sM}^{rD} ($\pm$0.0075).

Savage et al. (2011) measured the Si isotope composition of coexisting olivine, clinopyroxene and plagioclase

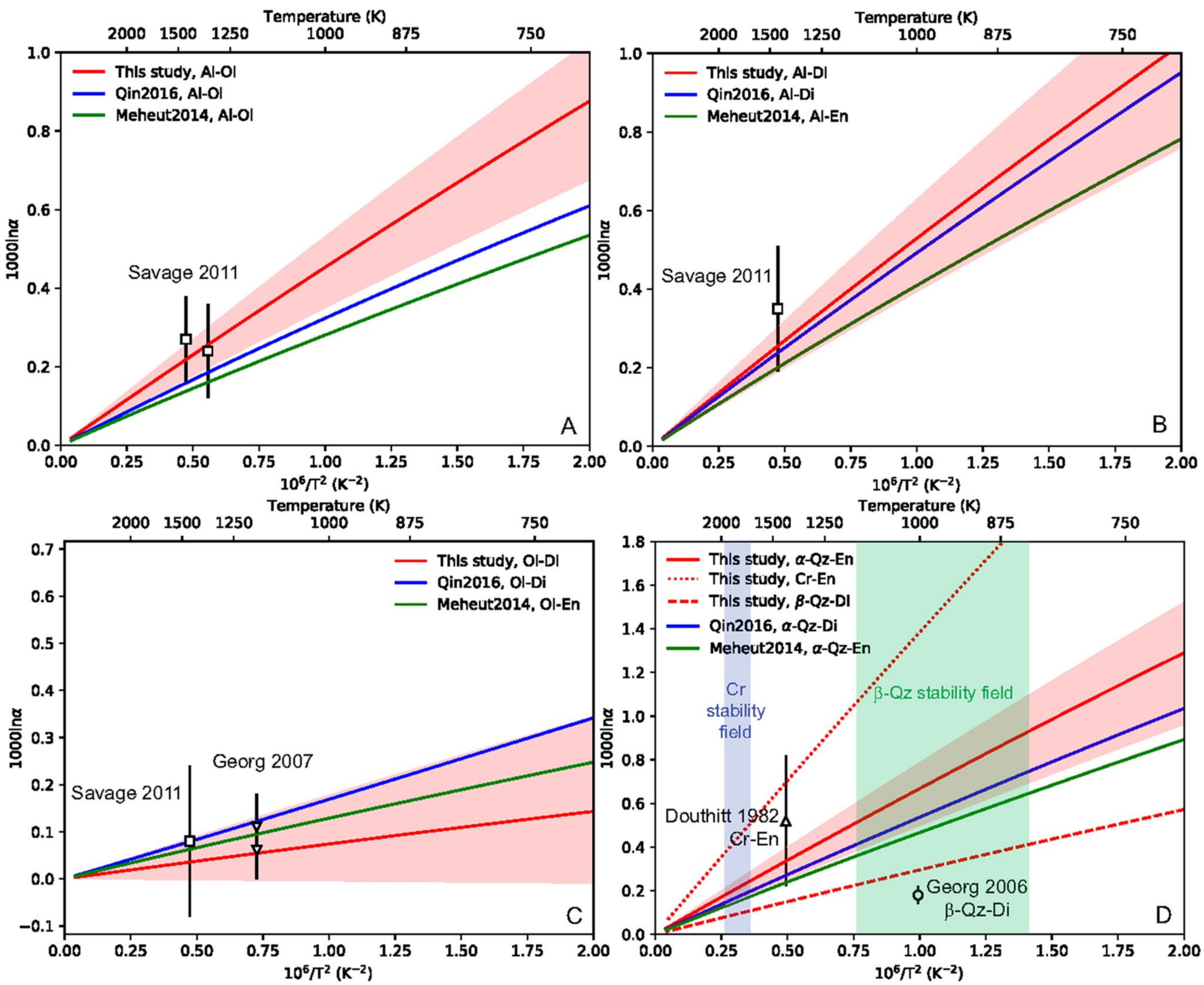

Fig. 5 Calculated $\ln\alpha_{Si30/28}$ between silicate minerals, compared to mass spectrometry measurements. Red curves: results from the *force constants* approach. Red shaded region indicates the uncertainty of the isotope fractionation from this study. Blue and green curves: results from DFT calculations. Symbols: results from mass spectrometry. **A** Albite–olivine system. Al: albite. Ol: olivine. **B** Albite–pyroxene system. Di: diopside. En: orthoenstatite. **C** Olivine–pyroxene system. **D** Silica–pyroxene system. Qz: quartz. Cr: cristobalite. For the sake of clarity, only the uncertainty of lnα between orthoenstatite and α-quartz is showed, and the other systems have uncertainties of similar magnitude. Blue shaded region: stability field of cristobalite. Green shaded region: stability field of β-quartz

separates from Skaergaard layered intrusion samples at different depths. The equilibrium temperatures of the layered intrusion samples were estimated to be 1340–1453 K based on the plagioclase compositions (Morse et al. 1980; Méheut and Schauble 2014). We compared the $\ln\alpha_{Si30/28}$ from our method with results from mass spectrometry and DFT calculations. In the albite–olivine system (Fig. 5A), our result is consistent with mass spectrometry measurements on Skaergaard mineral separates (Savage et al. 2011), and slightly higher than DFT calculations (Méheut and Schauble 2014; Qin et al. 2016). Similar situation occurs to albite–pyroxene system (Fig. 5B), where our result is slightly higher than DFT calculations (Méheut and Schauble 2014; Qin et al. 2016), while slightly lower than mass spectrometry measurements (Savage et al. 2011), and the uncertainties of different methods overlap.

For olivine–pyroxene system (Fig. 5C), Georg et al. (2007) measured the isotopic composition of two olivine-diopside pairs in Cameroon Line spinel-lherzolite mantle xenoliths. Though Georg et al. (2007) did not estimate the equilibrium temperature of the sample, Nkouandou and Temdjim (2011) estimated the equilibrium temperature for spinel lherzolite xenoliths from Ngao Volgar volcano, one of the Cameroon Line volcanos, to be ~900 °C. Combining the mass spectrometry results from Georg et al. (2007) and Savage et al. (2011), at ~1000 °C, there is a very small silicon isotope fractionation effect between olivine and pyroxene ($\ln\alpha_{Si30/28\ Ol-Py} \approx 0.08‰$). Our method gives a $\ln\alpha_{Si30/28}$ that is compatible with the DFT calculations and mass spectrometry measurements (Georg et al. 2007; Savage et al. 2011; Méheut and Schauble 2014; Qin et al. 2016). Our results confirms conclusions from previous studies that heavy silicon isotope prefers olivine over pyroxene, though the $\ln\alpha_{Si30/28}$ is very close to 0 over the temperature range of geological interest.

A more interesting case is the silica–pyroxene system (Fig. 5D). Douthitt (1982) estimated the equilibrium Si isotope fractionation between lunar cristobalite and clinopyroxene as $\ln\alpha_{Si30/28\ Cr-Py} = 0.52 \pm 0.3‰$ at an estimated equilibrium temperature of 1150 °C. The $\ln\alpha_{Si30/28}$ was determined based on previous gas source mass spectrometry results (Epstein and Taylor 1970, 1971, 1972, 1973; Taylor and Epstein 1973), and the equilibrium temperature was estimated based on the oxygen isotope fractionation (Douthitt 1982). The estimated $\ln\alpha_{Si30/28}$ value is higher than the results from DFT calculations between α-quartz and pyroxenes (Méheut et al. 2009; Méheut and Schauble 2014; Qin et al. 2016), though the errors overlap. Our calculation suggests that the $\ln\beta_{Si30/28}$ of cristobalite is much larger than the $\ln\beta_{Si30/28}$ of α-quartz, and the high $\ln\alpha_{Si30/28}$ value between lunar cristobalite and clinopyroxene should come from the high β-factor of cristobalite. If we assume the equilibrium $\ln\alpha_{Si30/28}$ between lunar cristobalite and lunar pyroxene is 0.52‰, based on our isotope fractionation curve (Fig. 5D, dotted curve), the calculated equilibrium temperature is 1400 °C, 250 °C higher than the estimation by Douthitt (1982). We note here that the stability field of cristobalite (1470–1705 °C, Heaney et al. (1994)) is higher than the estimated cristobalite-pyroxene equilibrium temperature (1150 °C, Douthitt (1982)), and it is possible that Douthitt (1982) underestimated the Si isotopic equilibrium temperature of lunar basalts. On the other hand, Georg (2006) measured silicon isotopic fractionation between quartz and diopside ($\ln\alpha_{Si30/28\ Qz-Di} = 0.18 \pm 0.04‰$) on a quartz-diopside marble of metamorphic origin (IL-14), whose equilibrium temperature is estimated as 730 °C (Valley and O'Neil 1984). The fractionation value of 0.18 ± 0.04‰ is much smaller than the calculated silicon isotope fractionation between α-quartz and pyroxene (Méheut et al. 2009). Méheut et al. (2009) concludes that the quartz–pyroxene samples in the IL-14 marble are not in equilibrium. Our calculation suggests that the $\ln\alpha_{Si30/28}$ between β-quartz and pyroxene is smaller than the $\ln\alpha_{Si30/28}$ between α-quartz and pyroxene. Since the temperature of 730 °C is in the stability field of β-quartz (573–870 °C, Heaney et al. (1994)), it is likely that the pyroxene sample in IL-14 marble is in equilibrium with β-quartz.

Application scope of the *force constants* approach

In this section, we would like to discuss the application scope of the *force constants* approach to constrain the isotope fractionation. As has been demonstrated in earlier sections, the calibration of C_{sM}^{rD} (Eq. 15) is based on the force constants of ^{IV}Si in SiO_4 tetrahedron in silicate minerals, so one cannot use this calibration to study minerals that contain six-coordinated Si in SiO_6 octahedron (^{VI}Si, e.g., bridgmanite, stishovite, and the six-coordinated Si in majorite). Nor can one use this calibration to determine the β-factor of silicon in iron-silicon alloys. The C_{sM}^{rD} for ^{VI}Si and Si in metal alloys needs to be calibrated in the future.

We explored the C_{sM}^{rD}-N_{rD} relationship of Fe, Mg and O in silicate minerals (Fig. 6). These elements also show trends with a positive slope between the C_{sM}^{rD} ratio and the resilience, yet the scattering of the data is significantly larger. The large scattering of C_{sM}^{rD} for ^{VI}Mg, ^{VI}Fe (Fig. 6A, B) and O (Fig. 6C) has different origins. ^{VI}Fe and ^{VI}Mg usually share the octahedral sites in crust and mantle silicates. Since Fe^{2+} and Mg^{2+} have very different number of electrons (24 vs. 10), the value of Debye–Waller factor of ^{VI}Fe and ^{VI}Mg is strongly correlated with the Fe-Mg occupancy in the octahedral site (Trueblood et al. 1996). At high temperatures, Fe^{2+} and Mg^{2+} cations diffuse and partition between different octahedral sites (Wang et al. 2005; Heinemann et al. 2007), and the partition coefficient (K_D) is a function of temperature. So at different

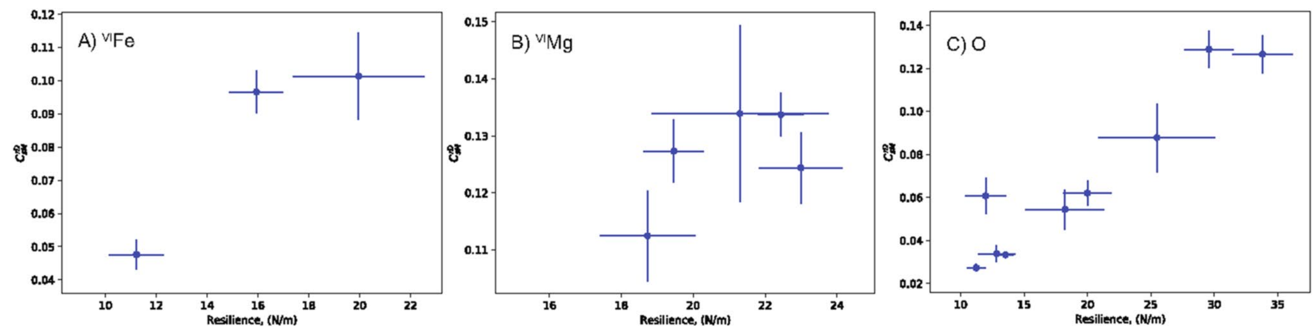

Fig. 6 C_{sM}^{rD}-N_{rD} relationship for **A** ^{VI}Fe, **B** ^{VI}Mg and **C** O^{2-} ions. The stiffness N_{sM} of ^{VI}Fe is experimentally determined from its NRXIS spectrum, while the N_{sM} of ^{VI}Mg and O^{2-} are fitted from DFT results using Eq. 8. All the N_{rD} and N_{sM} values are averaged among all iron/magnesium/oxygen sites in each mineral. Source of data: ^{VI}Fe: Smyth and Hazen (1973), Yang and Ghose (1995), Heinemann et al. (2006, 2007), Jackson et al. (2009), Dauphas et al. (2012, 2014), ^{VI}Mg: Cameron et al. (1973), Smyth and Hazen (1973), Hazen (1976), Yang and Ghose (1995), Heinemann et al. (2006, 2007), Schauble (2011), Huang et al. (2013), Wu et al. (2015), O^{2-}: Cameron et al. (1973), Smyth and Hazen (1973), Hazen (1976), Kihara (1990), Yang and Ghose (1995), Heinemann et al. (2006, 2007) Nakatsuka et al. (2011), Méheut et al. (2009); Méheut and Schauble (2014), Blanchard et al. (2015), Wu et al. (2015), Qin et al. (2016)

temperatures, the octahedral sites in silicate minerals usually have different Fe/Mg ratios (occupancy disorder), which leads to a change in the electron density and hence influences the N_{rD}. On the other hand, SiO_4 tetrahedral sites in silicate minerals are either dominantly occupied by Si^{4+}, or sometimes shared between Si^{4+} and Al^{3+} (e.g., albite), which have the same amount of electrons, so their occupancy disorder does not influence the determination of the Debye–Waller factor. So the C_{sM}^{rD}-N_{rD} relationship of ^{IV}Si shows a better confined linear trend than the C_{sM}^{rD}-N_{rD} relationship of ^{VI}Fe and ^{VI}Mg.

Theoretical calculations have demonstrated that the local chemical environments (e.g., bond length, polyhedral volume and polyhedral distortion) have strong effect on the force constants of ions in mineral (Méheut and Schauble 2014; Qin et al. 2016), and hence influence their β-factors. In most anhydrous silicates, O^{2-} is the only anion, and usually serves as the corners of atomic polyhedra. O^{2-} forms bonds with different cations while not having a consistent local chemical environment, so different oxygen sites in minerals could have distinct resiliences. For example, in the orthoenstatite sample that we measured in this study (Table 2), the maximum and minimum N_r of different oxygen sites have an 18% difference (22.1 N/m vs. 18.7 N/m), whereas the N_r of the two silicon sites only have 1.7% difference (27.9 N/m vs. 27.4 N/m). In crust and upper mantle minerals, Si usually exists in the form of Si^{4+} cation and occupies SiO_4 tetragonal sites. The SiO_4 tetragonal sites are small, and heavy elements are usually excluded from the tetragonal sites. So in the crust and upper mantle minerals, the Si^{4+} cation usually has a more consistent local chemical environment than the other cations or anions. The consistent local chemical environment makes ^{IV}Si the most suitable element to be studied by our *force constants* approach.

Conclusions

In this manuscript, we present a new *force constants* approach to constrain the equilibrium isotope fractionation β-factor of ^{IV}Si in the crust and upper mantle minerals. We extract the atomic mean square displacement $\langle u^2 \rangle$ from the Debye–Waller factor of ^{IV}Si derived from single crystal X-ray diffraction, and then calculate the resilience N_{rD} from the temperature dependence of $\langle u^2 \rangle$. With the calibrated relationship between the N_{rD} and the C_{sM}^{rD} (Eq. 15), we calculate the uncorrected stiffness N_{sM} of the ^{IV}Si in the mineral. The N_{sM} is then corrected with the ECoN to get the N_{sMC}. While the correction based on ECoN is minor for most minerals, we notice that the correction is most pronounced for pyroxenes ($\sim 2\%$). N_{sMC} is then used to calculate the β-factor (Eq. 8). One can calculate the isotope fractionation α-factor by taking the ratio of β-factor between different minerals.

We have compared the $\ln\alpha_{Si30/28}$ between minerals calculated from our *force constants* approach with the $\ln\alpha_{Si30/28}$ determined from DFT calculations and mass spectrometry. Our result is consistent with previous studies on the equilibrium isotope fractionation $\ln\alpha_{Si30/28}$ between olivine, albite and pyroxenes. Our calculations suggest that cristobalite, α-quartz and β-quartz have distinct β-factors, and studies on the equilibrium isotope fractionation of Si that involve silica should take into account of the different polymorphs. By combining our calculated $\ln\alpha_{Si30/28}$ and the phase diagram of silica, we suggest that the Si isotopic equilibrium temperature between cristobalite and pyroxene in lunar basalt was underestimated by ~250 °C (Douthitt 1982), and the pyroxene sample in IL-14 marble is in equilibrium with β-quartz (Georg 2006). The application of the resilience-stiffness calibration presented in this study should be confined to ^{IV}Si. Generalization of the *force constants* approach to

Si with different coordination numbers and other elements will require more experimental and theoretical studies in the future.

Supplementary Information The online version contains supplementary material available at https://doi.org/10.1007/s00410-021-01820-6.

Acknowledgements This work was performed at GeoSoilEnviroCARS (Sector 13), Partnership for Extreme Crystallography program (PX2), Advanced Photon Source (APS), and Argonne National Laboratory. GeoSoilEnviroCARS is supported by the National Science Foundation-Earth Sciences (EAR-1634415) and Department of Energy-Geosciences (DE-FG02-94ER14466). PX2 program is supported by COMPRES under NSF Cooperative Agreement EAR-1661511. Use of the Advanced Photon Source was supported by the U.S. Department of Energy, Office of Science, Office of Basic Energy Sciences, under Contract No. DE-C02-6CH11357. DZ acknowledges Dr. Merlin Méheut for kindly sending data from his paper. We thank the reviewers for their constructive comments, which help to improve this manuscript.

References

Bigeleisen J, Mayer MG (1947) Calculation of equilibrium constants for isotopic exchange reactions. J Chem Phys 15(5):261–267. https://doi.org/10.1063/1.1746492

Blanchard M, Dauphas N, Hu M, Roskosz M, Alp E, Golden D, Sio C, Tissot F, Zhao J, Gao L, Morris R, Fornace M, Floris A, Lazzeri M, Balan E (2015) Reduced partition function ratios of iron and oxygen in goethite. Geochim Cosmochim Acta 151:19–33. https://doi.org/10.1016/j.gca.2014.12.006. http://www.sciencedirect.com/science/article/pii/S0016703714007157

Blöchl PE (1994) Projector augmented-wave method. Phys Rev B 50:17953–17979. https://doi.org/10.1103/PhysRevB.50.17953. https://link.aps.org/doi/10.1103/PhysRevB.50.17953

Bourdon B, Roskosz M, Hin RC (2018) Isotope tracers of core formation. Earth-Sci Rev 181:61–81. https://doi.org/10.1016/j.earscirev.2018.04.006. http://www.sciencedirect.com/science/article/pii/S0012825217305792

Brown P, Fox A, Maslen E, O'Keefe M, Willis B (2006) Intensity of diffracted intensities. Int Tables Crystallogr C:554–595

Cameron M, Sueno S, Prewitt CT, Papike JJ (1973) High-temperature grystal ghemistry of acmite, diopside, hedenbergite, jadeite, spodumene, and ureyite. Am Miner 58:594–618

Coppens P (2010) The structure factor. Int Tables Crystallogr B:10–23

Corso AD (2014) Pseudopotentials periodic table: from h to pu. Comput Mater Sci 95:337–350. https://doi.org/10.1016/j.commatsci.2014.07.043. http://www.sciencedirect.com/science/article/pii/S0927025614005187

Dauphas N, Roskosz M, Alp EE, Golden DC, Sio CK, Tissot FLH, Hu MY, Zhao J, Gao L, Morris RV (2012) A general moment NRIXS approach to the determination of equilibrium Fe isotopic fractionation factors: application to goethite and jarosite. Geochim Cosmochim Acta 94:254–275

Dauphas N, Roskosz M, Alp E, Neuville D, Hu M, Sio C, Tissot F, Zhao J, Tissandier L, Médard E, Cordier C (2014) Magma redox and structural controls on iron isotope variations in earth's mantle and crust. Earth Planet Sci Lett 398:127–140. https://doi.org/10.1016/j.epsl.2014.04.033. http://www.sciencedirect.com/science/article/pii/S0012821X14002738

Dauphas N, Poitrasson F, Burkhardt C, Kobayashi H, Kurosawa K (2015) Planetary and meteoritic mg/si and δ^{30}si variations inherited from solar nebula chemistry. Earth Planet Sci Lett 427:236–248. https://doi.org/10.1016/j.epsl.2015.07.008. http://www.sciencedirect.com/science/article/pii/S0012821X15004355

Dauphas N, Hu MY, Baker EM, Hu J, Tissot FLH, Alp EE, Roskosz M, Zhao J, Bi W, Liu J, Lin JF, Nie NX, Heard A (2018) SciPhon: a data analysis software for nuclear resonant inelastic X-ray scattering with applications to Fe, Kr, Sn, Eu and Dy. J Synchrotron Radiat 25(5):1581–1599. https://doi.org/10.1107/S1600577518009487

Debye P (1913) Uber die intensitatsverteilung in den mit rontgenstrahlen erzeugten interferenzbildern. Verh Dtsch Phys Ges 15:738–752

Dolomanov OV, Bourhis LJ, Gildea RJ, Howard JAK, Puschmann H (2009) OLEX2: a complete structure solution, refinement and analysis program. J Appl Crystallogr 42(2):339–341. https://doi.org/10.1107/S0021889808042726

Douthitt C (1982) The geochemistry of the stable isotopes of silicon. Geochim Cosmochim Acta 46(8):1449–1458. https://doi.org/10.1016/0016-7037(82)90278-2. http://www.sciencedirect.com/science/article/pii/0016703782902782

Dunitz JD, Maverick EF, Trueblood KN (1988) Atomic motions in molecular crystals from diffraction measurements. Angew Chem Int Ed Engl 27(7):880–895 https://doi.org/10.1002/anie.198808801. https://onlinelibrary.wiley.com/doi/abs/10.1002/anie.198808801

Epstein S, Taylor HP (1970) $^{18}O/^{16}O$, $^{30}Si/^{28}Si$, D/H, and $^{13}C/^{12}C$ studies of lunar rocks and minerals. Science 167(3918):533–535. https://doi.org/10.1126/science.167.3918.533. http://science.sciencemag.org/content/167/3918/533. http://science.sciencemag.org/content/167/3918/533.full.pdf

Epstein S, Taylor HP (1971) $^{18}O/^{16}O$, $^{30}Si/^{28}Si$, D/H, and $^{13}C/^{12}C$ ratios in lunar samples. Proc 2nd Lunar Sci Conf Houston 2:1421–1441

Epstein S, Taylor HP (1972) $^{18}O/^{16}O$, $^{30}Si/^{28}Si$, $^{13}C/^{12}C$ and D/H studies of Apollo 14 and 15 samples. Proc 3rd Lunar Sci Conf Houston 2:1429–1454

Epstein S, Taylor HP (1973) $^{18}O/^{16}O$, $^{30}Si/^{28}Si$, $^{13}C/^{12}C$, D/H and hydrogen and carbon concentration data on apollo 11 soils. Eos 54:585–586

Fitoussi C, Bourdon B (2012) Silicon isotope evidence against an enstatite chondrite earth. Science 335(6075):1477–1480. https://doi.org/10.1126/science.1219509. http://science.sciencemag.org/content/335/6075/1477. http://science.sciencemag.org/content/335/6075/1477.full.pdf

Fitoussi C, Bourdon B, Kleine T, Oberli F, Reynolds BC (2009) Si isotope systematics of meteorites and terrestrial peridotites: implications for mg/si fractionation in the solar nebula and for si in the earth's core. Earth Planet Sci Lett 287(1):77–85. https://doi.org/10.1016/j.epsl.2009.07.038. http://www.sciencedirect.com/science/article/pii/S0012821X09004543

Georg R (2006) Geochemistry of stable silicon isotopes measured by high-resolution multi-collector inductively-coupled-plasma mass-spectrometry (hr-mc-icpms). PhD thesis, Ph.D. thesis, Swiss Federal institute of Technology Zuerich

Georg RB, Halliday AN, Schauble EA, Reynolds BC (2007) Silicon in the earth's core. Nature 447(7148):1102

Giannozzi P, Baroni S, Bonini N, Calandra M, Car R, Cavazzoni C, Ceresoli D, Chiarotti GL, Cococcioni M, Dabo I, Corso AD, de Gironcoli S, Fabris S, Fratesi G, Gebauer R, Gerstmann U, Gougoussis C, Kokalj A, Lazzeri M, Martin-Samos L, Marzari N, Mauri F, Mazzarello R, Paolini S, Pasquarello A, Paulatto L, Sbraccia C, Scandolo S, Sclauzero G, Seitsonen AP, Smogunov A, Umari P, Wentzcovitch RM (2009) QUANTUM ESPRESSO: a modular and open-source software project for quantum simulations of materials. J Phys: Condens Matter 21(39):395502. https://doi.org/10.1088/0953-8984/21/39/395502

Giannozzi P, Andreussi O, Brumme T, Bunau O, Nardelli MB, Calandra M, Car R, Cavazzoni C, Ceresoli D, Cococcioni M, Colonna N, Carnimeo I, Corso AD, de Gironcoli S, Delugas P, DiStasio RA, Ferretti A, Floris A, Fratesi G, Fugallo G, Gebauer R, Gerstmann U, Giustino F, Gorni T, Jia J, Kawamura M, Ko HY, Kokalj A, Küçükbenli E, Lazzeri M, Marsili M, Marzari N, Mauri F, Nguyen NL, Nguyen HV, de-la Roza AO, Paulatto L, Poncé S, Rocca D, Sabatini R, Santra B, Schlipf M, Seitsonen AP, Smogunov A, Timrov I, Thonhauser T, Umari P, Vast N, Wu X, Baroni SS (2017) Advanced capabilities for materials modelling with quantum ESPRESSO. J Phys: Condens Matter 29(46):465901. https://doi.org/10.1088/1361-648x/aa8f79

Gillet P, McMillan P, Schott J, Badro J, Grzechnik A (1996) Thermodynamic properties and isotopic fractionation of calcite from vibrational spectroscopy of 18o-substituted calcite. Geochim Cosmochim Acta 60(18):3471–3485. https://doi.org/10.1016/0016-7037(96)00178-0. http://www.sciencedirect.com/science/article/pii/0016703796001780

Hazen RM (1976) Effects of temperature and pressure on the cell dimension and x-ray temperature factors of periclase. Am Miner 61(3):266–71

Heaney PJ, Prewitt CT, Gibbs GV (1994) Silica: physical behavior, geochemistry, and materials applications. De Gruyter. https://doi.org/10.1515/9781501509698

Heinemann R, Kroll H, Kirfel A, Barbier B (2006) Order and anti-order in olivine i: structural response to temperature. Eur J Mineral 18(6):673–689

Heinemann R, Kroll H, Kirfel A, Barbier B (2007) Order and anti-order in olivine iii: variation of the cation distribution in the fe, mg olivine solid solution series with temperature and composition. Eur J Mineral 19(1):15–27

Hin RC, Coath CD, Carter PJ, Nimmo F, Lai YJ, von Strandmann PAP, Willbold M, Leinhardt ZM, Walter MJ, Elliott T (2017) Magnesium isotope evidence that accretional vapour loss shapes planetary compositions. Nature 549(7673):511

Hoppe R (1979) Effective coordination numbers (econ) and mean fictive ionic radii (mefir). Zeitschrift für Kristallographie-Crystalline Materials 150(1–4):23–52

Hoppe R, Voigt S, Glaum H, Kissel J, Müller HP, Bernet K (1989) A new route to charge distributions in ionic solids. J Less Common Metals 156(1):105–122. https://doi.org/10.1016/0022-5088(89)90411-6. http://www.sciencedirect.com/science/article/pii/0022508889904116

Hu MY, Toellner TS, Dauphas N, Alp EE, Zhao J (2013) Moments in nuclear resonant inelastic X-ray scattering and their applications. Phys Rev B 87:064301. https://doi.org/10.1103/PhysRevB.87.064301. https://link.aps.org/doi/10.1103/PhysRevB.87.064301

Huang F, Chen L, Wu Z, Wang W (2013) First-principles calculations of equilibrium mg isotope fractionations between garnet, clinopyroxene, orthopyroxene, and olivine: implications for mg isotope thermometry. Earth Planet Sci Lett 367:61–70. https://doi.org/10.1016/j.epsl.2013.02.025. http://www.sciencedirect.com/science/article/pii/S0012821X13000927

Huang F, Wu Z, Huang S, Wu F (2014) First-principles calculations of equilibrium silicon isotope fractionation among mantle minerals. Geochim Cosmochim Acta 140:509–520

Jackson JM, Palko JW, Andrault D, Sinogeikin SV, Lakshtanov DL, Wang J, Bass JD, ZHA CS, (2003) Thermal expansion of natural orthoenstatite to 1473 K. Eur J Mineral 15(3):469–473. https://doi.org/10.1127/0935-1221/2003/0015-0469. https://pubs.geoscienceworld.org/eurjmin/article-pdf/15/3/469/3121400/469.pdf

Jackson JM, Hamecher EA, Sturhahn W (2009) Nuclear resonant x-ray spectroscopy of (mg,fe)sio_3 orthoenstatites. Eur J Mineral 21(3):551–560. https://doi.org/10.1127/0935-1221/2009/0021-1932. https://www.ingentaconnect.com/content/schweiz/ejm/2009/00000021/00000003/art00003

Javoy M, Kaminski E, Guyot F, Andrault D, Sanloup C, Moreira M, Labrosse S, Jambon A, Agrinier P, Davaille A, Jaupart C (2010) The chemical composition of the earth: enstatite chondrite models. Earth Planet Sci Lett 293(3):259–268. https://doi.org/10.1016/j.epsl.2010.02.033. http://www.sciencedirect.com/science/article/pii/S0012821X10001445

Kieffer SW (1982) Thermodynamics and lattice vibrations of minerals: 5. applications to phase equilibria, isotopic fractionation, and high-pressure thermodynamic properties. Rev Geophys 20(4):827–849. https://doi.org/10.1029/RG020i004p00827. https://agupubs.onlinelibrary.wiley.com/doi/abs/10.1029/RG020i004p00827. https://agupubs.onlinelibrary.wiley.com/doi/pdf/10.1029/RG020i004p00827

Kihara K (1990) An X-ray study of the temperature dependence of the quartz structure. Eur J Mineral pp 63–78

Kuhs W (2013) Atomic displacement parameters. Int Tables Crystallogr D:231–245

Leu BM, Sage JT (2016) Stiffness, resilience, compressibility. Hyperfine Interact 237(1):87

Meagher EP (1975) The crystal structures of pyrope and grossularite at elevated temperatures. Am Miner 60(3–4):218–228

Méheut M, Schauble EA (2014) Silicon isotope fractionation in silicate minerals: insights from first-principles models of phyllosilicates, albite and pyrope. Geochim Cosmochim Acta 134:137–154

Méheut M, Lazzeri M, Balan E, Mauri F (2007) Equilibrium isotopic fractionation in the kaolinite, quartz, water system: Prediction from first-principles density-functional theory. Geochim Cosmochim Acta 71(13):3170–3181. https://doi.org/10.1016/j.gca.2007.04.012. http://www.sciencedirect.com/science/article/pii/S0016703707001858

Méheut M, Lazzeri M, Balan E, Mauri F (2009) Structural control over equilibrium silicon and oxygen isotopic fractionation: A first-principles density-functional theory study. Chem Geol 258(1):28–37. https://doi.org/10.1016/j.chemgeo.2008.06.051. http://www.sciencedirect.com/science/article/pii/S0009254108002738, applications of non-traditional stable isotopes in high-temperature geochemistry

Momma K, Izumi F (2011) VESTA3 for three-dimensional visualization of crystal, volumetric and morphology data. J Appl Crystallogr 44(6):1272–1276. https://doi.org/10.1107/S0021889811038970

Morse S, Lindsley D, Williams R (1980) Concerning intensive parameters in the Skaergaard intrusion. Am J Sci 280A:159–170

Nakatsuka A, Shimokawa M, Nakayama N, Ohtaka O, Arima H, Okube M, Yoshiasa A (2011) Static disorders of atoms and experimental determination of debye temperature in pyrope: Low-and high-temperature single-crystal x-ray diffraction study. Am Miner 96(10):1593–1605

Nespolo M, Ferraris G, Ohashi H (1999) Charge distribution as a tool to investigate structural details: meaning and application to pyroxenes. Acta Crystallogr B 55(6):902–916. https://doi.org/10.1107/S0108768199008708

Nkouandou OF, Temdjim R (2011) Petrology of spinel lherzolite xenoliths and host basaltic lava from ngao voglar volcano, adamawa massif (cameroon volcanic line, west africa): equilibrium conditions and mantle characteristics. J Geosci 56(4):375–387

Norris CA, Wood BJ (2017) Earth's volatile contents established by melting and vaporization. Nature 549(7673):507

O'Neill B (2014) Some useful moment results in sampling problems. Am Stat 68(4):282–296. https://doi.org/10.1080/00031305.2014.966589

Parak F, Knapp EW (1984) A consistent picture of protein dynamics. Proc Natl Acad Sci 81(22):7088–7092. http://www.pnas.org/content/81/22/7088.abstract. http://www.pnas.org/content/81/22/7088.full.pdf

Parak F, Hartmann H, Aumann KD, Reuscher H, Rennekamp G, Bartunik H, Steigemann W (1987) Low temperature x-ray investigation of structural distributions in myoglobin. Eur Biophys J 15(4):237–249. https://doi.org/10.1007/BF00577072

Parak F, Heidemeier J, Nienhaus GU (1988) Protein structural dynamics as determined by mössbauer spectroscopy. Hyperfine Interact 40(1–4):147–157

Pauling L (1929) The principles determining the structure of complex ionic crystals. J Am Chem Soc 51(4):1010–1026. https://doi.org/10.1021/ja01379a006

Pavese A, Artioli G, Prencipe M (1995) X-ray single-crystal diffraction study of pyrope in the temperature range 30–973 k. Am Miner 80(5–6):457–464

Peacor Peacor DB (1973) High-temperature single-crystal study of the cristobalite inversion. Zeitschrift für Kristallographie-Crystall Mater 138(1–6):274–298

Perdew JP, Burke K, Ernzerhof M (1996) Generalized gradient approximation made simple. Phys Rev Lett 77:3865–3868. https://doi.org/10.1103/PhysRevLett.77.3865. https://link.aps.org/doi/10.1103/PhysRevLett.77.3865

Polyakov V, Mineev S, Clayton R, Hu G, Gurevich V, Khramov D, Gavrichev K, Gorbunov V, Golushina L (2005) Oxygen isotope fractionation factors involving cassiterite (sno2): I. calculation of reduced partition function ratios from heat capacity and x-ray resonant studies. Geochim Cosmochim Acta 69(5):1287–1300. https://doi.org/10.1016/j.gca.2004.08.034. http://www.sciencedirect.com/science/article/pii/S001670370400688X

Polyakov VB (1998) On anharmonic and pressure corrections to the equilibrium isotopic constants for minerals. Geochim Cosmochim Acta 62(18):3077–3085

Polyakov VB (2009) Equilibrium iron isotope fractionation at core-mantle boundary conditions. Science 323(5916):912–914

Polyakov VB, Mineev SD (2000) The use of mössbauer spectroscopy in stable isotope geochemistry. Geochim Cosmochim Acta 64(5):849–865. https://doi.org/10.1016/S0016-7037(99)00329-4. http://www.sciencedirect.com/science/article/pii/S0016703799003294

Polyakov VB, Clayton RN, Horita J, Mineev SD (2007) Equilibrium iron isotope fractionation factors of minerals: reevaluation from the data of nuclear inelastic resonant X-ray scattering and Mössbauer spectroscopy. Geochim Cosmochim Acta 71(15):3833–3846

Prewitt C, Sueno S, Papike J (1976) The crystal structures of high albite and monalbite at high temperatures. Am Miner 61(11–12):1213–1225

Qin T, Wu F, Wu Z, Huang F (2016) First-principles calculations of equilibrium fractionation of o and si isotopes in quartz, albite, anorthite, and zircon. Contrib Miner Petrol 171(11):91

Savage PS, Georg RB, Williams HM, Burton KW, Halliday AN (2011) Silicon isotope fractionation during magmatic differentiation. Geochim Cosmochim Acta 75(20):6124–6139. https://doi.org/10.1016/j.gca.2011.07.043, http://www.sciencedirect.com/science/article/pii/S0016703711004418

Schauble E, Rossman G, Taylor H (2001) Theoretical estimates of equilibrium fe-isotope fractionations from vibrational spectroscopy. Geochim Cosmochim Acta 65(15):2487–2497. https://doi.org/10.1016/S0016-7037(01)00600-7. http://www.sciencedirect.com/science/article/pii/S0016703701006007

Schauble E, Rossman GR, Taylor HP (2004) Theoretical estimates of equilibrium chromium-isotope fractionations. Chem Geol 205(1):99–114. https://doi.org/10.1016/j.chemgeo.2003.12.015. http://www.sciencedirect.com/science/article/pii/S0009254103004005

Schauble EA (2004) Applying stable isotope fractionation theory to new systems. Rev Mineral Geochem 55(1):65–111. https://doi.org/10.2138/gsrmg.55.1.65. https://dx.doi.org/10.2138/gsrmg.55.1.65. https://pubs.geoscienceworld.org/rimg/article-pdf/55/1/65/2944515/65.gsrmg.55.pdf

Schauble EA (2011) First-principles estimates of equilibrium magnesium isotope fractionation in silicate, oxide, carbonate and hexaaquamagnesium(2+) crystals. Geochim Cosmochim Acta 75(3):844–869. https://doi.org/10.1016/j.gca.2010.09.044. http://www.sciencedirect.com/science/article/pii/S0016703710006332

Schauble EA, Rossman GR, Taylor H (2003) Theoretical estimates of equilibrium chlorine-isotope fractionations. Geochim Cosmochim Acta 67(17):3267–3281. https://doi.org/10.1016/S0016-7037(02)01375-3. http://www.sciencedirect.com/science/article/pii/S0016703702013753, a Special Issue Dedicated to Robert Clayton

Seiler P, Martinoni B, Dunitz JD (1984) Can x-ray diffraction distinguish between protium and deuterium atoms? Nature 309(5967):435

Shahar A, Ziegler K, Young ED, Ricolleau A, Schauble EA, Fei Y (2009) Experimentally determined si isotope fractionation between silicate and fe metal and implications for earth's core formation. Earth Planet Sci Lett 288(1):228–234. https://doi.org/10.1016/j.epsl.2009.09.025. http://www.sciencedirect.com/science/article/pii/S0012821X09005597

Sheldrick GM (2008) A short history of SHELX. Acta Crystallogr A Found Crystallogr 64(1):112–122

Singwi KS, Sjölander A (1960) Resonance absorption of nuclear gamma rays and the dynamics of atomic motions. Phys Rev 120:1093–1102

Smyth JR, Hazen RM (1973) The crystal structures of forsterite and hortonolite at several temperatures up to 900" c. Am Miner 58:588–593

Sturhahn W, Chumakov A (1999) Lamb-mössbauer factor and second-order doppler shift from inelastic nuclear resonant absorption. Hyperfine Interact 123(1–4):809–824

Taylor HP, Epstein S (1973) Oxygen and silicon isotope ratios of the luna 20 soil. Geochim Cosmochim Acta 37(4):1107–1109. https://doi.org/10.1016/0016-7037(73)90204-4. http://www.sciencedirect.com/science/article/pii/0016703773902044

Togo A, Tanaka I (2015) First principles phonon calculations in materials science. Script Mater 108:1–5. https://doi.org/10.1016/j.scriptamat.2015.07.021. http://www.sciencedirect.com/science/article/pii/S1359646215003127

Trueblood KNKN, Bürgi HB, Burzlaff H, Dunitz JD, Gramaccioli CM, Schulz HH, Shmueli U, Abrahams SC (1996) Dispacement parameter nomenclature. Report of a subcommittee on atomic displacement parameter nomenclature. Acta Crystallogr A 52(5):770–781. https://doi.org/10.1107/S0108767396005697

Urey HC (1947) The thermodynamic properties of isotopic substances. J Chem Soc pp 562–581. https://doi.org/10.1039/JR9470000562

Valley JW, O'Neil JR (1984) Fluid heterogeneity during granulite facies metamorphism in the adirondacks: stable isotope evidence. Contrib Miner Petrol 85(2):158–173. https://doi.org/10.1007/BF00371706

Wang L, Moon N, Zhang Y, Dunham WR, Essene EJ (2005) Fe–mg order-disorder in orthopyroxenes. Geochim Cosmochim Acta 69(24):5777–5788. https://doi.org/10.1016/j.gca.2005.08.011. http://www.sciencedirect.com/science/article/pii/S0016703705007003

Watkin D (2008) Structure refinement: some background theory and practical strategies. J Appl Crystallogr 41(3):491–522. https://doi.org/10.1107/S0021889808007279

Wehinger B, Bosak A, Refson K, Mirone A, Chumakov A, Krisch M (2015) Lattice dynamics of α-cristobalite and the boson peak in silica glass. J Phys: Condens Matter 27(30):305401. https://doi.org/10.1088/0953-8984/27/30/305401

Wilson AJC (1949) The probability distribution of X-ray intensities. Acta Crystallogr A 2(5):318–321. https://doi.org/10.1107/S0365110X49000813

Winter J, Ghose S, Okamura F (1977) A high-temperature study of the thermal expansion and the anisotropy of the sodium atom in low albite. Am Miner 62(9–10):921–931

Wu Z, Huang F, Huang S (2015) Isotope fractionation induced by phase transformation: first-principles investigation for mg 2 sio 4. Earth Planet Sci Lett 409:339–347

Yang H, Ghose S (1995) A transitional structural state and anomalous fe–mg order-disorder in mg-rich orthopyroxene,(mg0. 75fe0. 25) 2si2o6. Am Miner 80(1–2):9–20

Zaccai G (2000) How soft is a protein? A protein dynamics force constant measured by neutron scattering. Science 288(5471):1604–1607

Zambardi T, Poitrasson F, Corgne A, Méheut M, Quitté G, Anand M (2013) Silicon isotope variations in the inner solar system: Implications for planetary formation, differentiation and composition. Geochim Cosmochim Acta 121:67–83. https://doi.org/10.1016/j.gca.2013.06.040. http://www.sciencedirect.com/science/article/pii/S001670371300375X

Zhang D, Dera PK, Eng PJ, Stubbs JE, Zhang JS, Prakapenka VB, Rivers ML (2017) High pressure single crystal diffraction at PX2̂. J Vis Exp 119:e54660

Zhang D, Jackson JM, Sturhahn W, Zhao J, Alp EE, Hu MY (2021) Measurements of the Lamb–Mössbauer factor at simultaneous high pressure-temperature conditions and estimates of the equilibrium isotopic fractionation of iron. Am Mineral Press. https://doi.org/10.2138/am-2021-7884